


Spin-Orbit-Torque Switching of Noncollinear Antiferromagnetic Antiperovskite Manganese Nitride Mn_3GaN

T. Hajiri[✉],* K. Matsuura, K. Sonoda, E. Tanaka, K. Ueda[✉], and H. Asano
Department of Materials Physics, Nagoya University, Nagoya 464-8603, Japan

 (Received 30 April 2021; accepted 21 July 2021; published 3 August 2021)

Noncollinear antiferromagnets have promising potential for replacing ferromagnets in the field of spintronics as high-density devices with ultrafast operation. To take full advantage of noncollinear antiferromagnets in spintronics applications, it is important to achieve efficient manipulation of noncollinear antiferromagnetic spin. Here, using the anomalous Hall effect as an electrical signal of the triangular magnetic configuration, spin-orbit-torque switching with no external magnetic field is demonstrated in noncollinear antiferromagnetic antiperovskite manganese nitride Mn_3GaN at room temperature. The pulse-width dependence and subsequent relaxation of Hall signal behavior indicate that the spin-orbit torque plays a more important role than the thermal contribution due to pulse injection. In addition, multistate memristive switching with respect to pulse current density is observed. The findings advance the effective control of noncollinear antiferromagnetic spin, facilitating the use of such materials in antiferromagnetic spintronics and neuromorphic computing applications.

DOI: [10.1103/PhysRevApplied.16.024003](https://doi.org/10.1103/PhysRevApplied.16.024003)

I. INTRODUCTION

Noncollinear antiferromagnetic (AFM) materials have attracted significant attention in basic and applied science because in addition to having the excellent properties of collinear AFM materials—such as fast dynamics, suitability for high-density integration, and stability against external perturbations—noncollinear AFM materials can overcome the weakness of collinear AFM materials—namely the small electrical signal—by the anomalous Hall effect (AHE) [1–4]. Thus, efficient control of noncollinear AFM spin is essential for the application of such materials in AFM spintronics. In the past decade, electrical manipulation via spin-transfer torque and spin-orbit torque (SOT) has become one of the most promising techniques in the field of ferromagnet (FM)-based spintronics, not only to take the place of dynamic random access memory in current computer memory hierarchy [5] but also to instantiate multistate magnetoresistive random access memories for neuromorphic computing [6,7].

Recent studies demonstrate that like collinear AFM materials, noncollinear AFM materials can be controlled via SOT in the same way as FM materials. Collinear AFM materials consisting of NiO/Pt bilayers and Pt/NiO/Pt trilayers show a critical current density (J_c) of the order of 10^7 – 10^8 A/cm² [8–10], similar to that in typical FM/heavy metal (HM) bilayers. In contrast, J_c values one to two orders of magnitude smaller have been observed in noncollinear AFM Mn_3GaN (MGN)/Pt bilayers ($1.5 \times$

10^6 A/cm²) [11] and $\text{Mn}_3\text{Sn/W}$ bilayers (5×10^6 A/cm²) [12]. In the case of a collinear AFM system, 90° switching of the Néel vector is required because the electrical signal, such as spin Hall magnetoresistance and anisotropic magnetoresistance, is maximal. To achieve 90° switching of the Néel vector, diagonal current flow using an eight- or four-terminal device with complex electrical write-read operation is required [8–10], except for CuMnAs using a two-terminal writing device [13]. A noncollinear AFM system, by contrast, needs 180° switching of each spin of triangular magnetic configuration, which can be accomplished using a simple four-terminal Hall device with no external magnetic field in Mn_3GaN [11], or with an external magnetic field in Mn_3Sn [12]. Therefore, in addition to their large electrical signals due to nonzero Berry curvature [14], noncollinear AFM systems have a distinct advantage in spintronic applications.

In the antiperovskite manganese nitrides Mn_3AN (where $A = \text{Ni, Ga, Sn, etc.}$), the Mn atoms form a kagome lattice in the (111) plane. The noncollinear AFM Mn_3AN with a nonzero Berry curvature has been predicted to exhibit a large AHE and an anomalous Nernst effect even with a quite small canted magnetization of the order of $(0.001$ – $0.01)\mu_B$ per atom [15–17]. The AHE has been established in $\text{Mn}_3\text{Ni}_{1-x}\text{Cu}_x\text{N}$ films [18,19], strained Mn_3NiN films [20], and strained Mn_3SnN films [21]. Although electrical current switching of both Hall resistance with no external magnetic field and nonlinear Hall resistance with respect to an external magnetic field have been reported in MGN/Pt bilayers, no clear evidence of AHE has yet been presented [11]. In addition, a

*t.hajiri@nagoya-u.jp

thermal contribution due to pulse current injection such as a thermal activation effect, a joule heating effect, or an electromigration effect can change the Hall resistance [22–24]. Hence, as has been pointed out, both the low-electrical-current writing and reading operations of MGN/Pt bilayers could be of nonmagnetic thermal origin [25].

In this investigation, we study the magnetotransport properties of MGN films and perform systematic switching operations of strained MGN/HM (HM = Pt, Ta) bilayers. At room temperature, no AHE is obtained in relaxed MGN films, whereas the AHE appears with respect to the ratio between the lattice constants c and a (c/a ratio). The temperature dependence of the magnetization and the AHE suggests that skew scattering is dominant below 200 K, whereas another origin, probably noncollinear AFM order with nonzero Berry curvature, is dominant above 200 K. To estimate the effect of thermal contributions on write–read operations, the pulse-width dependence and relaxation after pulse injection are measured. We show that the thermal activation effect, joule heating effect, and electromigration effect play a minor role. The existence of multistate signal amplitude with respect to pulse current with no external magnetic field is demonstrated.

II. EXPERIMENTAL DETAILS

MGN films are grown by reactive magnetron sputtering on MgO(001) substrates using a Mn₃Ga target at 400 °C.

As details of the film growth were reported in our previous work, the c/a ratio is controlled by precise control of N₂ partial pressure during film growth [26]. The crystal structure is analyzed using both in-plane and out-of-plane X-ray diffraction (XRD) measurements with Cu $K\alpha$ radiation. Magnetic properties are characterized using superconducting quantum interference device magnetometry. Transport properties are characterized by the standard dc four-terminal method. For write–read operations, a layer of Pt or Ta (3 nm) is deposited by magnetron sputtering at room temperature after film growth. Hall bars of 20 μm in width with Ti/Cu contact pads are prepared by a conventional photolithographic process. All SOT measurements are performed with no external magnetic field at room temperature (300 K). The sequence of write–read operations is the same as described in our previous report [11].

III. RESULTS AND DISCUSSION

A. Film characteristics and magnetotransport properties

Typical out-of-plane 2θ – ω and in-plane 2θ – ϕ XRD patterns for the 35-nm-thick MGN films are shown in Fig. 1(a). Only the MGN (002) and (200) planes exhibit Bragg peaks, in the out-of-plane and in-plane XRD patterns, respectively. In addition, epitaxial growth is confirmed by the results of ϕ -scan measurement as shown

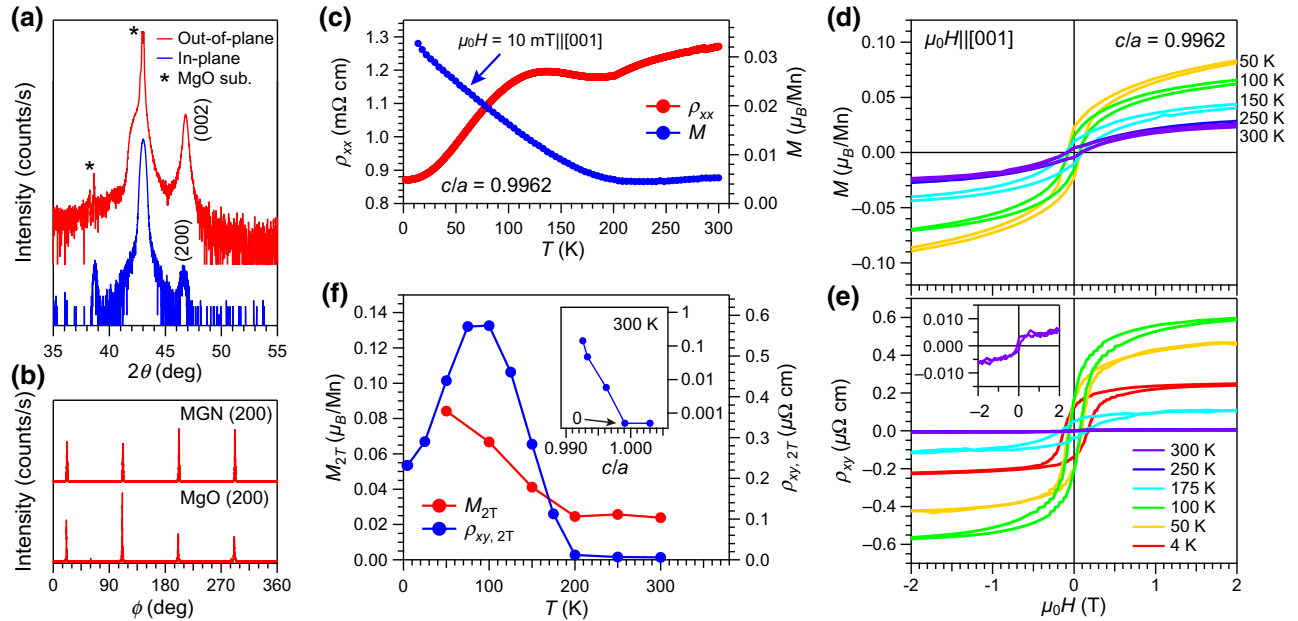


FIG. 1. (a) Out-of-plane and in-plane XRD profiles for MGN films around (002) and (200) peaks. (b) In-plane ϕ scans of MGN films. (c) Temperature (T) dependence of the resistivity ρ_{xx} and magnetization M of MGN films. For the magnetization measurement, an external magnetic field $\mu_0 H$ of 10 mT is applied parallel to the [001] direction. (d) Out-of-plane magnetic hysteresis loops and (e) anomalous Hall resistivity loops for MGN films at various temperatures. Inset of (e) is an enlargement of the anomalous Hall resistivity loop at 300 K. (f) Out-of-plane magnetization at 2 T and anomalous Hall resistivity $\rho_{xy, 2T}$ at 2 T for MGN films as a function of temperature. The inset presents the anomalous Hall resistivity at 300 K as a function of the c/a ratio. The $c/a = 0.9962$ film is 35-nm thick, while other films are 50-nm thick.

in Fig. 1(b), showing that their epitaxial relationship is MgO(001)[100]//MGN(001)[100]. The lattice constants c and a are 0.388 17 and 0.389 65 nm, respectively, giving $c/a = 0.9962$. The temperature dependencies of the resistivity ρ_{xx} and magnetization M are shown in Fig. 1(c). In the ρ_{xx} curve, there is a clear anomaly at 200 K. Likewise, a FM-like transition is observed at 200 K in the magnetization curve. These temperature dependencies were also observed in our previous switching study of MGN/Pt films [11]. The ground state of MGN at room temperature is well known to exhibit Γ_{5g} spin structure [27]. The coexistence of Γ_{5g} and M-1 phase below the FM-like transition temperature has also been previously reported [28]. As the MGN/FM bilayers exhibit an exchange bias at 4 K [29], it is concluded that Γ_{5g} order and M-1 phase coexist below 200 K.

Figures 1(d) and 1(e) show the magnetic M hysteresis and anomalous Hall resistivity ρ_{xy} loops for the MGN films measured along the $\langle 001 \rangle$ direction at various temperatures. In the ρ_{xy} loops, linear contribution from the ordinary Hall effect has been subtracted. The ρ_{xy} loops before subtracting the ordinary Hall effect and a summary of the Hall coefficient values are given in Fig. 6 of Appendix A. In both loops, hysteresis is clearly exhibited not only in the coexistence phase below 200 K but also in the Γ_{5g} single phase. Both the magnetization and the ρ_{xy} loops of the MGN films have similar coercive field (H_c) values, indicating that the AHE is directly related to the MGN magnetic order. The temperature dependencies of the magnetization and ρ_{xy} at 2 T are shown in Fig. 1(f). Above 200 K, the magnetization remains nearly constant at approximately $0.02 \mu_B/\text{Mn}$; below 200 K, it increases monotonically with decreasing temperature. ρ_{xy} , on the other hand, increases slightly with decreasing temperature above 200 K and increases dramatically with decreasing temperature below 200 K, indicating that the increase in ρ_{xy} is strongly linked to the increase in magnetization. In contrast to the magnetization, however, ρ_{xy} begins to decrease below 75 K. As ρ_{xy} is found to be proportional to ρ_{xx} below 75 K, ρ_{xy} below 200 K would be dominated by a net magnetization.

According to theoretical studies on piezomagnetism of MGN with Γ_{5g} order, a net magnetization can appear by the induction of strain [30,31], and the magnitude of the net magnetization increases linearly with respect to the strain $\epsilon\%$, with a coefficient of $0.013 \mu_B/\text{Mn}/\%$ [30]. Our MGN films show ϵ and remnant magnetization of approximately 0.3% and $0.004 \mu_B/\text{Mn}$ at 300 K, respectively. As the net magnetization observed in our MGN films is similar to the value calculated theoretically, it is considered that the canted Γ_{5g} order is realized above 200 K. The Γ_{5g} order does not show the AHE because it has mirror symmetry, and the symmetry operations make the Berry curvature vanish after integration over the entire Brillouin zone [15]. In antiperovskite nitride films with Γ_{5g} order, however, the anomalous Hall conductivity tensor is

reported to be highly sensitive to strain. Although strain-free Mn₃NiN films show no AHE [18], strained Mn₃NiN films do show AHE [20]. This is explained by the reduction of the symmetry of a space group, under which nonzero Berry curvature is induced when a finite strain is applied [20]. Strained Mn₃SnN films likewise show a large AHE, but it is suggested that the biaxial strain induces Γ_{4g} order from Γ_{5g} order [21]. These past findings indicate that AHE cannot be accounted for by either extrinsic scattering processes or changes in magnetization; hence, nonzero Berry curvature plays an important role. In our MGN films, ρ_{xy} is observed to increase with decreasing c/a ratio at 300 K as shown in the inset of Fig. 1(f), highlighting the fact that appearance of AHE at 300 K in MGN films is also strongly related to the film strain and/or reduced magnetic space group. Therefore, although we cannot experimentally separate the contributions from canted net magnetization and nonzero Berry curvature due to noncollinear AFM order above 200 K, we can state that part of the AHE comes from noncollinear AFM order. From the viewpoint of SOT, we discuss the possible origin of AHE in a later section.

B. Dependence of reversible electrical switching on HM

For the electrical write–read operations, typical Hall bar devices of bilayers consisting of strained MGN (20 nm) with either Pt or Ta (3 nm) of $20 \mu\text{m}$ in width are prepared. From a parallel circuit model, the ρ_{xx} values for both the MGN/Pt and MGN/Ta bilayers can be derived using ρ_{xx} of each single-layer film, which enable us to estimate current density through the Pt and Ta layers ($J_{c,\text{HM}}$). The ρ_{xx} values at 300 K for MGN, Pt, and Ta single-layer films and MGN/Pt and MGN/Ta bilayers are given in Table I. Using these bilayers, sequential write–read operations are performed, with the results as shown in Fig. 2. Here, the top and bottom axes are the current densities derived from the Pt/Ta layer alone and the bilayer total thickness, respectively, and the left and right axes are the ρ_{xy} values derived from the full bilayer and the MGN layer alone, respectively. In addition, the constant offset probably due to geometrical imperfections of the Hall bar and/or thermoelectric voltage is subtracted. ρ_{xy} changes with respect to J , and a clear hysteresis loop is observed in both bilayers at 300 K with no external magnetic field, indicating success of the electrical write–read operation. The critical current densities J_c ($J_{c,\text{HM}}$) for MGN/Pt and MGN/Ta are obtained as $2.72 \times 10^6 \text{ A/cm}^2$ ($13.13 \times 10^6 \text{ A/cm}^2$) and $4.81 \times 10^6 \text{ A/cm}^2$ ($6.13 \times 10^6 \text{ A/cm}^2$), respectively. Theoretically, J_c would be proportional to θ_{HM}^{-1} , where θ_{HM} is the spin Hall angle of the HM layer [32]. We find that the ratio $J_{c,\text{Pt}} : J_{c,\text{Ta}} = 2.1 : 1$ is nearly equal to the ratio $|\theta_{\text{Pt}}|^{-1} : |\theta_{\text{Ta}}|^{-1} = 1.9 : 1$, indicating that spin current generated in the HM layer plays an important role. We note that the different ρ_{xy} switching width between MGN/Pt and

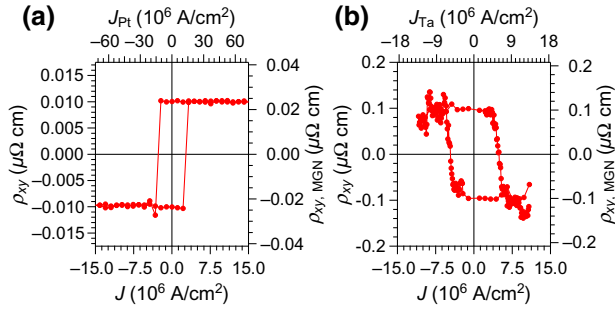


FIG. 2. Sequential electrical current switching for (a) MGN/Pt and (b) MGN/Ta bilayers with no external magnetic field at room temperature. The current density J is derived by the total thickness of the bilayers, and the current density through the HM layer J_{HM} is derived by HM thickness and the current through the HM layer as estimated using a parallel circuit model. In the same manner, ρ_{xy} and $\rho_{xy,\text{MGN}}$ are derived by the total thickness of bilayers and by MGN thickness and the current through the MGN layer.

MGN/Ta devices is probably due to local variations in the quality and/or strain of the thin films, which is discussed in Fig. 7 of Appendix B. Besides, the comparison of ρ_{xy} width between field-sweep and SOT measurements using the same device is presented in Fig. 8 of Appendix C.

To evaluate the effect of joule heating by applying pulse current, the pulse-width dependence is investigated. Figure 3(a) shows ρ_{xy} as a function of J with several pulse widths for MGN/Ta bilayers. Although the switching ρ_{xy} amplitudes remain nearly the same, the hysteresis loops become slightly narrower with increasing pulse width. J_c is plotted as a function of pulse width in Fig. 3(b). Here, J_c is fitted by the thermal activation model [33]:

$$J_c = J_{c0} \left[1 - \frac{1}{\Delta} \ln \left(\frac{\tau}{\tau_0} \right) \right], \quad (1)$$

where J_{c0} is the critical current density at 0 K, Δ is the thermal stability factor, and τ_0^{-1} is the thermally activated switching frequency, for which we assume a frequency of $1/\tau_0 = 1$ THz. It can be seen that J_c can be fitted by the thermal activation model with $J_{c0} = 7.97 \times 10^6$ A/cm²

TABLE I. Resistivities of Mn₃GaN, Pt, and Ta single-layer films, and Mn₃GaN/Pt and Mn₃GaN/Ta bilayers at 300 K. The resistivities of Mn₃GaN/Pt and Mn₃GaN/Ta bilayers are calculated using a parallel circuit model from the corresponding single-layer resistivities.

Film	ρ_{xx} ($\mu\Omega$ cm)
Mn ₃ GaN	1271
Pt	112
Ta	972
Mn ₃ GaN/Pt	504 (exp.), 541 (calc.)
Mn ₃ GaN/Ta	1261 (exp.), 1222 (calc.)

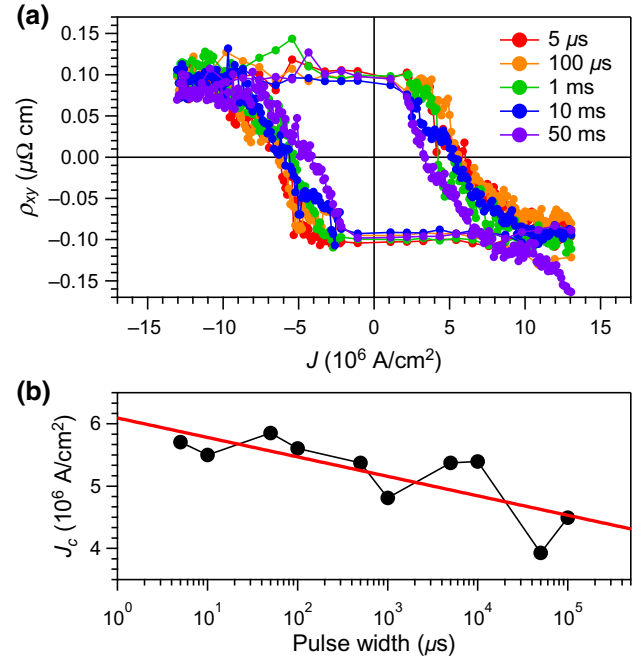


FIG. 3. (a) ρ_{xy} as a function of J observed for several pulse widths in MGN/Ta bilayers with no external magnetic field at room temperature. (b) Critical current density J_c as a function of pulse width. The bold solid line is the result of a fit to a thermal activation model.

and $\Delta = 58.7$. These results highlight the finding that a J_c value of the order of 10^6 A/cm² originates intrinsically in spin torque, whereas the thermal activation, through it exists, plays a minor role.

C. Thermal contribution to write-read operations

Because heating and electromigration effects can affect ρ_{xy} signal amplitudes [23], the relaxation behavior after switching is investigated. Figure 4 presents the continuous write-read operation using $I_{\text{pulse}} = \pm 13 \times 10^6$ A/cm² with a 5- μ s pulse width and subsequent relaxation measurements for MGN/Ta bilayers at 300 K. Figure 4(b) is an enlargement of the continuous $\pm I_{\text{pulse}}$ write part shown in Fig. 4(a). As discussed for synthetic AFM materials [34] and in our previous MGN/Pt study [11], the observed asymptotic ρ_{xy} behavior can be fitted by an exponential decay function $y = y_0 + A \exp[-(x + x_0)/\tau]$ with time constants τ of 14.9 pulse number (197.0 s) for $+I_{\text{pulse}}$ and 15.7 pulse number (207.6 s) for $-I_{\text{pulse}}$ with continuous write-read operations in approximately 13.25-s cycles. The relaxation behavior after switching is measured after three cycles of the continuous $\pm I_{\text{pulse}}$ write operations.

Figure 4(c) presents the ρ_{xy} relaxation as a function of time after continuous $\pm I_{\text{pulse}}$ write operations. The

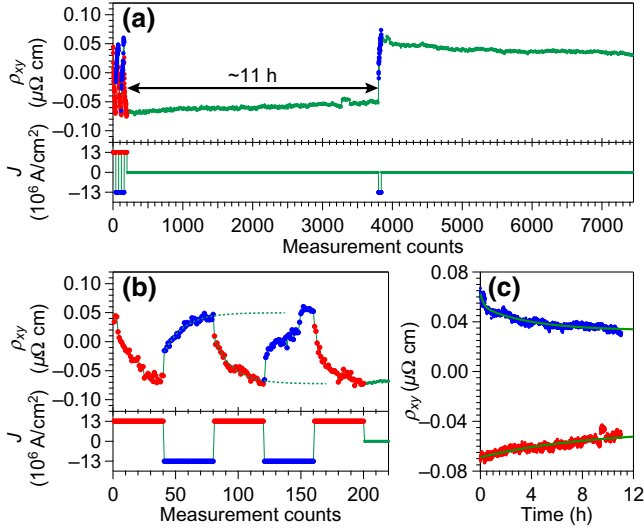


FIG. 4. (a) Continuous write-read operations and subsequent relaxation measurements with no external magnetic field at room temperature. (b) Continuous write-read operation part from (a). The dashed lines are the results of a fit to the exponential decay function. (c) Relaxation measurement parts from (a). The bold solid lines are the results of a fit to the double-exponential function.

relaxation behavior is characterized by a fit to a double-exponential function [23]:

$$d = d_0 + d_1 \exp\left(-\frac{t}{\tau_1}\right) + d_2 \exp\left(-\frac{t}{\tau_2}\right), \quad (2)$$

where d_0 is a base line and is the value reached when attenuated, d_1 , d_2 are amplitude parameters, and τ_1 , τ_2 are the relaxation times. Both relaxations after $\pm I_{\text{pulse}}$ write operations fit well with $d_0 = -0.0467 \mu\Omega \text{ cm}$, $d_1 = -0.0219 \mu\Omega \text{ cm}$, $d_2 = -0.0003 \mu\Omega \text{ cm}$, $\tau_1 = 8.63 \text{ h}$, $\tau_2 = 11.67 \text{ h}$ for after the $+I_{\text{pulse}}$ write operation, and $d_0 = 0.0331 \mu\Omega \text{ cm}$, $d_1 = 0.0100 \mu\Omega \text{ cm}$, $d_2 = 0.0194 \mu\Omega \text{ cm}$, $\tau_1 = 0.25 \text{ h}$, $\tau_2 = 3.89 \text{ h}$ for after the $-I_{\text{pulse}}$ write operation. With regard to the change in Hall resistance due to the effects of annealing and electromigration, the short and long decay times are reported to be approximately 4 and 50 min, respectively [23]. Compared with these values, both the short and long decay times observed here are 5 to 10 times longer. In addition, for the change in Hall resistance due to annealing and electromigration effects, the Hall resistance asymptotes to the initial value before pulse injection is a few minutes to a few hours [23,35], in contrast with our MGN/Ta bilayers, for which d_0 is a rather large value. Whereas our electrical measurements do not enable us to fully distinguish SOT and other possible contributions such as thermal activation and electromigration effects, the relaxation behavior and pulse-width behavior in the MGN/Ta bilayers highlight the fact that SOT

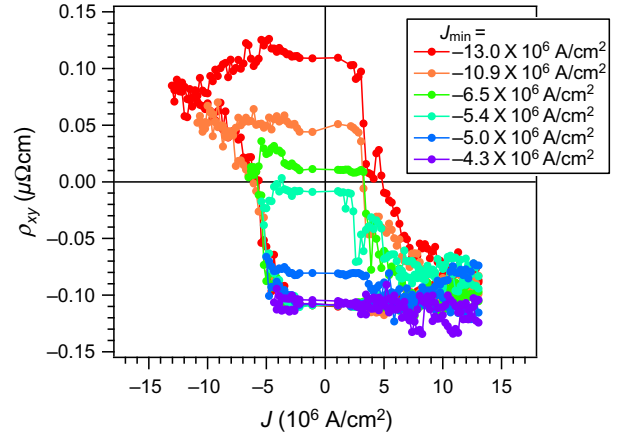


FIG. 5. Dependence of ρ_{xy} - J loops on J_{min} for MGN/Ta bilayers with no external magnetic field at room temperature.

plays an important role in the present switching behavior. In the case of collinear AFM materials such as NiO, 90° switching of the Néel vector is required, which can be achieved by the flow of current in two orthogonal directions. However, current flow in orthogonal directions causes inhomogeneous current density due to the current crowding effect, which induces a change in Hall resistance due to annealing and electromigration effect [23]. In the case of noncollinear AFM materials, in contrast, 180° switching of each noncollinear spin is required, which can be achieved by the flow of current in a straight line; this implies that the current crowding effect in this study can be considered small.

D. Memristive switching with respect to pulse current density

Finally, here we discuss the memristive behavior of MGN/Ta bilayers. Figure 5 shows ρ_{xy} - J loops at 300 K, where $J_{\text{max}} = 13.0 \times 10^6 \text{ A/cm}^2$ is first applied and subsequently scanned from J_{max} to J_{min} and from J_{min} to J_{max} . ρ_{xy} exhibits multiple stable signal amplitudes according to the magnitude of J_{min} . The same behavior has been observed in $\text{Mn}_3\text{Sn/Pt}$ bilayers [12] and AFM/FM bilayers [36], suggesting that the phenomenon of multiple stable magnitudes of the Hall resistance originates in the multi-AFM domain character, which allows us to tune the signal amplitude in an analog manner. In contrast to $\text{Mn}_3\text{Sn/Pt}$ bilayers [12], MGN/Ta bilayers show a memristive behavior with no external magnetic field, highlighting the advantage of Mn_3AN systems for use in neuromorphic computing.

According to theoretical study of SOT of Γ_{4g} order, the noncollinear spins rotate in the (111) plane of the kagome lattice, where the injected spins are directed perpendicular to the kagome lattice. Therefore, J_c is determined by an in-plane anisotropic energy of the kagome lattice and the injected spin direction. Further improvements in SOT

efficiency in noncollinear Mn_3AN systems may be realized using (110)-oriented films of low-anisotropy materials. Theoretically, $\text{Mn}_3\text{Ga}_{1-x}\text{Ni}_x\text{N}$ [37] has a low anisotropy energy, implying that it would be worthwhile to investigate the dependence of SOT efficiency on A atoms. On the other hand, if the AHE comes from only net magnetization (for simplicity, assume a net magnetization in the perpendicular direction as in a ferrimagnet), the magnetic field parallel to the current direction is generally needed to realize the SOT switching. In contrast, SOT of noncollinear AFM systems is theoretically satisfied even though with no external magnetic field [32,37]. Indeed, no switching has been observed with no external magnetic field at low temperatures where the ferrimagnetic M1 phase is dominant in the AHE [11]. Although joule heating can affect the Hall resistivity, the pulse-width measurement and relaxation measurement show a heating effect plays a minor role. From these results, we can conjecture that the AHE is possibly related to noncollinear AFM order from the viewpoint of SOT at 300 K.

IV. CONCLUSION

In this study, we show the AHE and SOT switching of noncollinear AFM MGN at room temperature. By tuning the c/a ratio, two origins of AHE are observed: one for AHE above 200 K, possibly related to noncollinear AFM order, and one for AHE below 200 K, dominated by magnetization. Using MGN/HM bilayers, we demonstrate the SOT switching of noncollinear AFM spin in MGN at room temperature with no external magnetic field. The effects of thermal activation on J_c and the effects of heating and electromigration on ρ_{xy} are excluded by pulse-width measurements and relaxation measurements after pulse injection. In addition, multistate memristive switching with respect to pulse current density is demonstrated. These results show that efficient SOT can be realized in MGN/HM bilayers with memristive functionality with no external magnetic field, and demonstrate the potential application in AFM spintronics and neuromorphic computing.

ACKNOWLEDGMENTS

This work is supported by the Japan Society for the Promotion of Science (KAKENHI Grants No. 20H02602 and No. 19K15445), Tokuyama Science Foundation, the Hori Science and Arts Foundation, and Kyosho Hatta Foundation. Part of this work was carried out under the Cooperative Research Project Program of the Research Institute of Electrical Communication, Tohoku University.

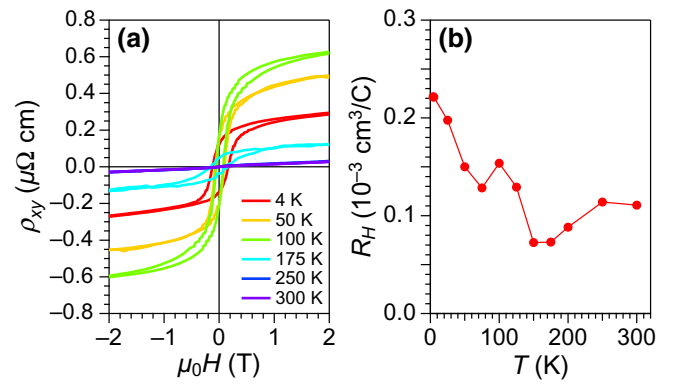


FIG. 6. (a) Hall resistivity ρ_{xy} as a function of external magnetic field for MGN films ($c/a = 0.9962$) before subtracting the ordinary Hall effect. (b) Temperature dependence of the Hall coefficient R_H .

APPENDIX A: ORDINARY HALL EFFECT OF MGN FILMS

Figure 6(a) shows the Hall resistivity ρ_{xy} as a function of external magnetic field for MGN films ($c/a = 0.9962$) at various temperatures before subtracting the ordinary Hall effect. The temperature dependence of the Hall coefficient R_H is summarized in Fig. 6(b).

APPENDIX B: SAMPLE DEPENDENCE OF ρ_{xy} SWITCHING WIDTH IN SOT MEASUREMENTS

Figure 7 shows the sample dependence of ρ_{xy} switching width in SOT measurements as a function of lattice constant c . The ρ_{xy} obtained by field-sweep measurements of unpatterned films is also plotted. While no ρ_{xy} switching is observed for samples with lattice constants c longer than 0.3890 nm, ρ_{xy} switching is observed in samples with shorter c , which is consistent with the results of AHE measurements of unpatterned films. On the other hand, although no large differences in c between 0.3882 and 0.3887 nm among SOT films in which ρ_{xy} switching are observed, ρ_{xy} switching width shows sample dependence. Since the amplitude of ρ_{xy} is strongly related to c/a ratio as discussed in the main text, the sample dependence of ρ_{xy} switching width is probably due to local variations in the quality and/or strain of the thin films.

APPENDIX C: COMPARISON OF ρ_{xy} WIDTH BETWEEN FIELD-SWEEP AND SOT MEASUREMENTS USING THE SAME DEVICE

Figure 8 shows the results of the Hall and SOT measurements using the same SOT device. Unfortunately, since our superconducting magnet has limited bore sizes, we cannot measure the AHE of SOT devices. On the other

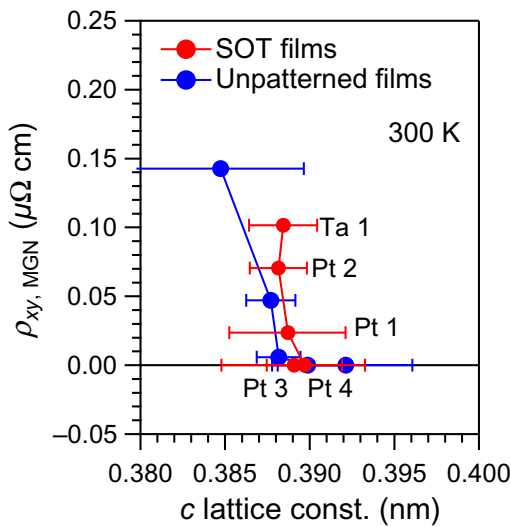


FIG. 7. Sample dependence of ρ_{xy} switching width in SOT measurements for MGN(20 nm)/HM(3 bn) bilayers. MGN/Pt and MGN/Ta results presented in the main text are the devices Pt1 and Ta1, respectively. For Pt2 device, $\rho_{xy, \text{MGN}}$ is derived by assuming that the current flows through MGN and Pt in the same proportion as in Pt1 device.

hand, as shown in Fig. 8(a), the nonlinear Hall effect is observed within the range ± 1.5 T in SOT devices [11]. Although the hysteresis is not observed probably due to insufficient magnetic field, we confirm that the change of Hall resistance R_{xy} is similar between field-sweep and SOT measurements in the same sample as shown in Fig. 8(b).

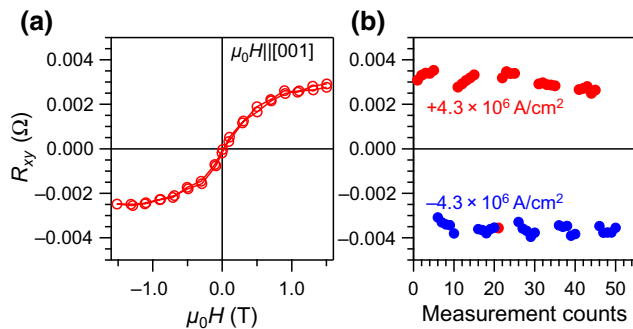


FIG. 8. Hall and SOT measurements using the same SOT device. (a) R_{xy} after subtracting estimated ordinary Hall effect versus external magnetic field of MGN/Pt bilayers. (b) R_{xy} versus pulse number of MGN/Pt bilayers. All measurements are performed at room temperature using the same MGN/Pt Hall device. The data are reproduced from *Appl. Phys. Lett.* **115**, 052403 (2019) [11], with the permission of AIP Publishing.

- [1] S. Nakatsuji, N. Kiyohara, and T. Higo, Large anomalous Hall effect in a non-collinear antiferromagnet at room temperature, *Nature* **527**, 212 (2015).
- [2] T. Jungwirth, X. Martí, P. Wadley, and J. Wunderlich, Antiferromagnetic spintronics, *Nat. Nanotechnol.* **11**, 231 (2016).
- [3] V. Baltz, A. Manchon, M. Tsoi, T. Moriyama, T. Ono, and Y. Tserkovnyak, Antiferromagnetic spintronics, *Rev. Mod. Phys.* **90**, 015005 (2018).
- [4] H. Bai, X. Zhou, Y. Zhou, X. Chen, Y. You, F. Pan, and C. Song, Functional antiferromagnets for potential applications on high-density storage and high frequency, *J. Appl. Phys.* **128**, 210901 (2020).
- [5] S. Bhatti, R. Sbiaa, A. Hirohata, H. Ohno, S. Fukami, and S. N. Piramanayagam, Spintronics based random access memory: A review, *Mater. Today* **20**, 530 (2017).
- [6] J. Grollier, D. Querlioz, K. Y. Camsari, K. Everschor-Sitte, S. Fukami, and M. D. Stiles, Neuromorphic spintronics, *Nat. Electron.* **3**, 360 (2020).
- [7] P. Rzeszut, J. Checiński, I. Brzozowski, S. Zietek, W. Skowroński, and T. Stobiecki, Multi-state MRAM cells for hardware neuromorphic computing, *ArXiv:2102.03415* (2021).
- [8] X. Z. Chen, R. Zarzuela, J. Zhang, C. Song, X. F. Zhou, G. Y. Shi, F. Li, H. A. Zhou, W. J. Jiang, F. Pan, and Y. Tserkovnyak, Antidamping-Torque-Induced Switching in Biaxial Antiferromagnetic Insulators, *Phys. Rev. Lett.* **120**, 207204 (2018).
- [9] L. Baldrati, O. Gomonay, A. Ross, M. Filianina, R. Lebrun, R. Ramos, C. Leveille, F. Fuhrmann, T. R. Forrest, F. Maccherozzi, S. Valencia, F. Kronast, E. Saitoh, J. Sinova, and M. Kläui, Mechanism of Néel Order Switching in Antiferromagnetic Thin Films Revealed by Magnetotransport and Direct Imaging, *Phys. Rev. Lett.* **123**, 177201 (2019).
- [10] T. Moriyama, K. Oda, T. Ohkochi, M. Kimata, and T. Ono, Spin torque control of antiferromagnetic moments in NiO, *Sci. Rep.* **8**, 14167 (2018).
- [11] T. Hajiri, S. Ishino, K. Matsuura, and H. Asano, Electrical current switching of the noncollinear antiferromagnet Mn_3GaN , *Appl. Phys. Lett.* **115**, 052403 (2019).
- [12] H. Tsai, T. Higo, K. Kondou, T. Nomoto, A. Sakai, A. Kobayashi, T. Nakano, K. Yakushiji, R. Arita, S. Miwa, Y. Otani, and S. Nakatsuji, Electrical manipulation of a topological antiferromagnetic state, *Nature* **580**, 608 (2020).
- [13] P. Wadley, S. Reimers, M. J. Grzybowski, C. Andrews, M. Wang, J. S. Chauhan, B. L. Gallagher, R. P. Campion, K. W. Edmonds, S. S. Dhesi, F. Maccherozzi, V. Novak, J. Wunderlich, and T. Jungwirth, Current polarity-dependent manipulation of antiferromagnetic domains, *Nat. Nanotechnol.* **13**, 362 (2018).
- [14] H. Chen, Q. Niu, and A. H. MacDonald, Anomalous Hall Effect Arising from Noncollinear Antiferromagnetism, *Phys. Rev. Lett.* **112**, 017205 (2014).
- [15] G. Gurung, D.-F. Shao, T. R. Paudel, and E. Y. Tsymbal, Anomalous Hall conductivity of noncollinear magnetic antiperovskites, *Phys. Rev. Mater.* **3**, 044409 (2019).
- [16] V. T. N. Huyen, M.-T. Suzuki, K. Yamauchi, and T. Oguchi, Topology analysis for anomalous Hall effect in the noncollinear antiferromagnetic states of Mn_3AN

- ($A = \text{Ni, Cu, Zn, Ga, Ge, Pd, In, Sn, Ir, Pt}$), *Phys. Rev. B* **100**, 094426 (2019).
- [17] I. Samathrakakis and H. Zhang, Tailoring the anomalous Hall effect in the noncollinear antiperovskite Mn_3GaN , *Phys. Rev. B* **101**, 214423 (2020).
- [18] K. Zhao, T. Hajiri, H. Chen, R. Miki, H. Asano, and P. Gegenwart, Anomalous Hall effect in the noncollinear antiferromagnetic antiperovskite $\text{Mn}_3\text{Ni}_{1-x}\text{Cu}_x\text{N}$, *Phys. Rev. B* **100**, 045109 (2019).
- [19] R. Miki, K. Zhao, T. Hajiri, P. Gegenwart, and H. Asano, Epitaxial growth and orientation-dependent anomalous Hall effect of noncollinear antiferromagnetic $\text{Mn}_3\text{Ni}_{0.35}\text{Cu}_{0.65}\text{N}$ films, *J. Appl. Phys.* **127**, 113907 (2020).
- [20] D. Boldrin, I. Samathrakakis, J. Zemen, A. Mihai, B. Zou, F. Johnson, B. D. Esser, D. W. McComb, P. K. Petrov, H. Zhang, and L. F. Cohen, Anomalous Hall effect in noncollinear antiferromagnetic Mn_3NiN thin films, *Phys. Rev. Mater.* **3**, 094409 (2019).
- [21] Y. You, H. Bai, X. Chen, Y. Zhou, X. Zhou, F. Pan, and C. Song, Room temperature anomalous Hall effect in antiferromagnetic Mn_3SnN films, *Appl. Phys. Lett.* **117**, 222404 (2020).
- [22] C. C. Chiang, S. Y. Huang, D. Qu, P. H. Wu, and C. L. Chien, Absence of Evidence of Electrical Switching of the Antiferromagnetic Néel Vector, *Phys. Rev. Lett.* **123**, 227203 (2019).
- [23] B. J. Jacot, G. Krishnaswamy, G. Sala, C. O. Avci, S. Vélez, P. Gambardella, and C.-H. Lambert, Systematic study of nonmagnetic resistance changes due to electrical pulsing in single metal layers and metal/antiferromagnet bilayers, *J. Appl. Phys.* **128**, 173902 (2020).
- [24] M. Meinert, D. Graulich, and T. Matalla-Wagner, Electrical Switching of Antiferromagnetic Mn_2Au and the Role of Thermal Activation, *Phys. Rev. Appl.* **9**, 064040 (2018).
- [25] H. Yan, Z. Feng, P. Qin, X. Zhou, H. Guo, X. Wang, H. Chen, X. Zhang, H. Wu, C. Jiang, and Z. Liu, Electric-field-controlled antiferromagnetic spintronic devices, *Adv. Mater.* **32**, 1905603 (2020).
- [26] S. Ishino, J. So, H. Goto, T. Hajiri, and H. Asano, Preparation and evaluation of $\text{Mn}_3\text{GaN}_{1-x}$ thin films with controlled N compositions, *AIP Adv.* **8**, 056312 (2018).
- [27] D. Fruchart and E. F. Bertaut, Magnetic studies of the metallic perovskite-type compounds of manganese, *J. Phys. Soc. Jpn.* **44**, 781 (1978).
- [28] K. Shi, Y. Sun, J. Yan, S. Deng, L. Wang, H. Wu, P. Hu, H. Lu, M. I. Malik, Q. Huang, and C. Wang, Baromagnetic effect in antiperovskite $\text{Mn}_3\text{Ga}_{0.95}\text{N}_{0.94}$ by neutron powder diffraction analysis, *Adv. Mater.* **28**, 3761 (2016).
- [29] T. Hajiri, H. Goto, and H. Asano, Scaling the electrical current switching of exchange bias in fully epitaxial antiferromagnet/ferromagnet bilayers, *Phys. Rev. B* **102**, 014404 (2020).
- [30] P. Lukashev, R. F. Sabirianov, and K. Belashchenko, Theory of the piezomagnetic effect in Mn-based antiperovskites, *Phys. Rev. B* **78**, 184414 (2008).
- [31] J. Zemen, Z. Gercsi, and K. G. Sandeman, Piezomagnetism as a counterpart of the magnetovolume effect in magnetically frustrated Mn-based antiperovskite nitrides, *Phys. Rev. B* **96**, 024451 (2017).
- [32] Y. Yamane, O. Gomonay, and J. Sinova, Dynamics of noncollinear antiferromagnetic textures driven by spin current injection, *Phys. Rev. B* **100**, 054415 (2019).
- [33] N. H. D. Khang, S. Nakano, T. Shirokura, Y. Miyamoto, and P. N. Hai, Ultralow power spin-orbit torque magnetization switching induced by a non-epitaxial topological insulator on Si substrates, *Sci. Rep.* **10**, 12185 (2020).
- [34] T. Moriyama, W. Zhou, T. Seki, K. Takahashi, and T. Ono, Spin-Orbit-Torque Memory Operation of Synthetic Antiferromagnets, *Phys. Rev. Lett.* **121**, 167202 (2018).
- [35] M. Dunz, T. Matalla-Wagner, and M. Meinert, Spin-orbit torque induced electrical switching of antiferromagnetic MnN, *Phys. Rev. Res.* **2**, 013347 (2020).
- [36] S. Fukami, C. Zhang, S. DuttaGupta, A. Kurenkov, and H. Ohno, Magnetization switching by spin-orbit torque in an antiferromagnet-ferromagnet bilayer system, *Nat. Mater.* **15**, 535 (2016).
- [37] G. Gurung, D.-Fu Shao, and E. Y. Tsymbal, Spin-torque switching of noncollinear antiferromagnetic antiperovskites, *Phys. Rev. B* **101**, 140405(R) (2020).